A hybrid probabilistic correction model for the state of charge estimation of lithium-ion batteries considering dynamic currents and temperatures.

TAKYI-ANINAKWA, P., WANG, S., ZHANG, H., YANG, X. and FERNANDEZ, C.

2023

A hybrid probabilistic correction model for the state of charge estimation of lithium-ion batteries considering dynamic currents and temperatures

Paul Takyi-Aninakwa[a], Shunli Wang[a*], Hongying Zhang[a], Yang Xiao[a], Carlos Fernandez[b]

[a] *School of Information Engineering, Southwest University of Science and Technology, Mianyang 621010, China*

[b] *School of Pharmacy and Life Sciences, Robert Gordon University, Aberdeen AB10-7GJ, UK.*

Abstract: Accurately estimating the state of charge (SOC) of lithium-ion batteries by the battery management system (BMS) is crucial for safe electric vehicle (EV) operations. This paper proposes a SOC estimation method for lithium-ion batteries based on a deep feed-forward neural network (DFFNN) optimized with a relevant attention mechanism and stochastic weight (RAS) algorithms. The relevant attention mechanism extracts useful features from the input data. Then, the stochastic weight algorithm randomly updates the weights and biases, rather than keeping them constant, for the DFFNN to estimate the SOC using full-scale input data and solve the gradient problem. To estimate the SOC by adaptively correcting each state's probability and error covariance quantities while maintaining robustness against spontaneous error noise and spikes, a shifting-step innovation unscented Kalman filter (SUKF) based on a Bayesian transformation is proposed. With its transfer learning mechanism, the RAS optimization solves the gradient problems and enhances the DFFNN's generalizability to various working conditions, providing more accurate estimates at a lower training cost. Furthermore, based on the findings and comparisons, the results of the proposed RAS-DFFNN-SUKF model show that it has the overall best mean absolute error, root mean square error, and mean absolute percentage error values of 0.03854%, 0.05238%, and 0.18853%, respectively, which shows that it is reliable and adaptable enough for practical BMS applications in EVs by ensuring fast and accurate SOC estimation.

Keywords: state of charge; lithium-ion battery; relevant attention mechanism; stochastic weight algorithm; deep feed-forward neural network; shifting-step innovation unscented Kalman filter

***Corresponding authors:** Shunli Wang E-mail address: wangshunli@swust.edu.cn

Abbreviation			
SOC	State of charge	RMSE	Root mean square error
EV	Electric vehicle	MAPE	Mean absolute percentage error
BMS	Battery management system	LiC	Lithium cobalt oxide
DFFNN	Deep feed-forward neural network	LiNCM	Lithium nickel cobalt manganese oxide
RAS	Relevant attention mechanism and stochastic weight algorithms	SUKF	Shifting-step innovation unscented Kalman filter
RT	Room temperature	DST	Dynamic stress test
ME	Maximum error	FUDS	Federal urban driving cycle
MAE	Mean absolute error	BBDST	Beijing bus dynamic stress test

1. Introduction

The industry and market share of this new mode of transportation have entered a prosperous period of rapid development as a result of the recent rapid expansion of the practicability and variety of electric vehicles (EVs) [1]. Therefore, the demand for rechargeable and high-performance batteries is on the rise. Power capacity has also grown exponentially, with 125 energy storage systems storing a total of 869 MW by the end of 2018, which is double the value reported in 2015. Out of all the different battery chemistries, lithium-ion batteries have been the most promising and competitive energy storage system. For instance, in 2018, lithium-ion batteries in the United States supplied over 90% of the large-scale battery storage power capacity [2, 3]. With unique features such as high energy and power densities, no memory effect, a low self-discharge rate, a long cycle life, being lightweight, having a wide operating temperature range, etc., lithium-ion batteries can achieve longer endurance and driving mileage and aid in the mitigation of global warming [4, 5].

Lithium-ion batteries offer a wide range of applications, including EVs, smart grids, mobile phones, e-scooters, laptops, etc. [6]. However, if the batteries are not properly monitored and controlled by a well-modeled battery management system (BMS), problems with safety, reliability, durability, and cost will arise due to the complex electrochemical nature and nonlinear working conditions encountered during EV operations [7, 8]. The BMS is an embedded electronic system that is integrated with rechargeable batteries to monitor vital data parameters. In EVs, it functions basically by monitoring the battery status, including

the current, voltage, temperature, etc. [9]. On the other hand, it also performs management tasks such as modeling, state estimation (state of charge (SOC), state of health estimation, state of energy, etc.), thermal regulation, cell balancing, fault diagnosis, etc. [10, 11].

As a fuel gauge functions in conventional vehicles, in EVs, the SOC represents the ratio of residual available capacity to maximum available capacity during the operating period [12]. Accurate estimation not only indicates how much capacity is available, but it also avoids unforeseen system interruptions and keeps the battery from being overcharged or over-discharged, which may cause permanent damage and largely reduce the battery life [13, 14]. With the measurable variables of current, voltage, and occasionally surface temperature serving as inputs for a robust estimation method, estimating the battery's SOC by the BMS has evolved into a crucial task to ensure safe and reliable system performance [15, 16].

1.1 *Classification of SOC estimation methods*

Currently, several SOC estimation methods have been introduced, which can be roughly divided into four categories: experimental methods, Coulomb counting method, model-based methods, and artificial intelligence methods [17-19]. Contrary to the other categories, the experiment methods, such as the open-circuit voltage [20] and electrochemical impedance spectroscopy method [21], are based on parameter characterization to provide online SOC estimation. However, it is still difficult to use and obtain accurate SOC results due to a variety of unfavorable factors, including lengthy resting periods, poor working conditions, inaccurate measuring tools, poor application ability, etc. [5, 22-24]. The Coulomb counting method is simple, has low computational complexity, and is widely used to estimate the SOC. However, the initial SOC, current measurement, and battery capacity inconsistencies have a significant impact on its accuracy [25].

In battery applications, the model-based SOC estimation method has been extensively used. First, battery models such as the equivalent circuit model [26], the physics-based electrochemical model [27], and the mechanistic model [28] are developed to monitor and simulate the dynamic behaviors of the battery. Based on any of the abovementioned battery models, model-based methods often use optimized Kalman

filtering algorithms, such as the extended Kalman filter [29, 30], the unscented Kalman filter (UKF) [31, 32], the particle filter [33, 34], the H-infinity filter [35, 36], etc. However, all of these approaches still share similar drawbacks, including the time-consuming computation complexities, thorough analysis of the chemical reactions taking place inside the battery, and the difficulty in adapting inadequate models or parameters to complex real-world working conditions [37, 38]. Other factors, such as irreversible battery aging and poor driving conditions, have a significant negative impact on SOC estimation, preventing their application and promotion in real-world EVs [39, 40].

In recent years, swift development has been made in the field of artificial intelligence. Artificial intelligence applications built on deep learning networks have numerous applications in different areas of study, including the implementation of BMS for EVs [41, 42]. Deep learning networks such as the deep feed-forward neural network (DFFNN), the long short-term memory neural network (LSTM), the gated recurrent unit (GRU), the convolutional neural network, and other neural networks have been employed for battery state estimation due to their superior nonlinear self-adaptation, self-learning, and high estimation accuracy [43, 44]. This method regards the lithium-ion battery as a "black box" rather than a mathematical estimation model that needs insight into the complicated electrochemical reactions inside the battery during the model's construction [45, 46].

1.2 *Literature review of SOC estimation methods*

Artificial intelligence-based SOC estimation techniques have been developed as a result of recent developments in deep learning networks. With a feed-forward mechanism, Vidal et al. [47] established a DFFNN for SOC estimation using batteries with two different chemistries. However, this study does not consider the critical temperature and charge-discharge rate effects on the battery. Darbar et al. [48] established the conventional DFF network for SOC at different charge-discharge current rates at room temperature (RT) conditions. Under RT conditions, Almaita et al. [49] established an LSTM for SOC estimation and compared its performance with that of the FF and DFF networks. However, actual EV battery driving profiles differ from these standard dynamic profiles because they can vary depending on

location, driver, and season [50]. Tian et al. [51] established a deep neural network-based method and used the KF method for optimization in estimating the SOC with only 10-min charging voltage and current input data, which ensures fast computation. However, a network trained using a few conventional profiles may not be able to guarantee accurate SOC estimation under various real-world EV driving circumstances due to the long operating distance and conditions [52].

SOC estimation has been accomplished with reasonable accuracy using recurrent neural network (RNN) variants. A denoising autoencoder (DAE), which extracts the pertinent battery data features for the GRU model for SOC estimation at RT under three working conditions, is proposed by Chen et al. [53]. Ren et al. [54] proposed a hybrid particle swarm optimization (PSO)-LSTM model and contrasted it with the LSTM model at RT for the estimation of the SOC under noise characterization. However, the critical nonlinear condition factors that affect the battery, such as temperature, charge-discharge rates, etc., are not taken into account [55]. Wang et al. [56] proposed an improved GRU-based TL for SOC estimation using small target sample datasets at temperatures ranging from 32 to 50 °C under three working conditions, which does not show the long-range SOC estimation ability and the robustness of the method at low temperatures [57]. For the short- and long-term estimation of SOC at the early stages of degradation at a temperature of 30 °C, Oyewole et al. [58] proposed a controllable deep transfer learning (CDTL) model using two LSTM models as the source and target cells. By enhancing the LSTM network, Ma et al. [59] proposed a sequence-to-sequence mapping model with a process information (SSMPI) model for SOC estimation. A two-stage pretraining strategy is used to improve the model's ability to learn new features at temperatures of 0, 25, and 45 °C. However, due to the advantages and disadvantages of one battery chemistry over the other under adverse operating conditions, it is necessary to consider these varieties to show the ability of the proposed to accurately estimate the SOC [60]. Furthermore, SOC estimation typically needs to be accomplished using a nonlinear function that varies, including subzero temperatures and different charge-discharge current rates [37].

1.3 *Problems and contributions of this paper*

An optimal architecture of the DFFNN is essential for faster convergence and better accuracy for SOC estimation of lithium-ion batteries. However, its training becomes tedious as the depth of the network increases due to several hyperparameters, such as the number of hidden layers, the number of hidden neurons in each hidden layer, the number of connections between layers, etc. The trial-and-error approach is used in establishing the optimal DFFNN architecture, which is an augmented combinatorial problem and a tedious task. To address this problem, the DFFNN with a transfer learning mechanism is optimized to automatically create an optimal architecture with enhanced accuracy and generalization ability. This paper aims to propose a relevant attention mechanism with input data feature extraction capabilities to extract the useful features in the input data. Then, to simultaneously optimize the weights and biases of the number of hidden layers and their respective neurons for the DFFNN to accurately estimate the SOC using large datasets, a stochastic weight algorithm based on a decomposition approach is established. (The relevant attention mechanism and stochastic weight algorithm are abbreviated as RAS). Then, an unscented Kalman filter with a shifting-step innovation (SUKF) is proposed based on the Bayesian transformation to optimize the state by adaptively correcting the probability of each state, error covariance, and noise covariance quantities while maintaining robustness against spontaneous error noise and spikes. This paper is based on the most popular constant current-constant voltage (CC-CV) charging method for EVs, which can easily be applied to other advanced charging strategies. The main benefits of the proposed strategy in this paper are highlighted as follows:

(1) From the aspect of method innovation, the relevant attention mechanism ensures efficient extraction of input data features. Also, the stochastic weight algorithm introduced into the DFFNN simultaneously optimizes the weights and biases of the various neurons rather than keeping them constant to avoid over-fitting, solve the gradient problems, and improve its transfer learning ability and robustness.

(2) From a practical perspective, the transfer learning mechanism of the DFFNN and RAS-DFFNN enables it to be trained on complex dynamic profiles and battery chemistries to achieve high accuracy SOC estimation with high generalization ability. Furthermore, the proposed RAS-DFFNN-SUKF model

quickly adapts to various operating conditions, including different temperatures, charge-discharge rates, cyclic test profiles, and battery chemistries, with less noise.

(3) Comparing the validation results, the RAS-DFFNN-SUKF model is superior and outperforms other existing SOC methods. The proposed method is a data-driven initialization approach, which eliminates the need for complicated battery models compared to equivalent methods like model-based methods.

1.4 *Organization of the paper*

The structure of the paper is organized as follows: Following the introduction in Section 1, Section 2 mathematically analyzes the SOC estimation and correction methods; Section 3 elucidates the battery tests and data collection as well as the results, discussion, and performance analysis; and Section 4 presents the conclusion and future work.

2. SOC estimation methods

2.1 *Feature-weighted relevant attention mechanism*

The collected data are fed into the developed relevant attention mechanism, which outputs into the stochastic weight-optimized DFFNN to estimate the SOC corresponding to the final sampling point. This paper employs the relevant attention mechanism as a feature extractor to select the relevant inherent features from the input data and ensure faster computation. It optimizes the network to adaptively select the relevant inherent features based on the attention weight, which is a key parameter used to estimate the correlation of the input relative to the estimated value attached to the input [52].

With a dense layer for the dynamic calculation of the attention weights, assuming $x_1, x_2, x_3, \dots, x_N$ are the input data, and $e_1, e_2, e_3, \dots, e_N$ are the featured attention weights. Based on *N*-dimensional features, the output of the stage attention-weighted $\tilde{x}_k$ is expressed in Equation (1).

$$\tilde{x}_k = \left(e_k^1 x_k^1, e_k^2 x_k^2, e_k^3 x_k^3, \dots, e_k^N x_k^N\right)^T \quad (1)$$

The dense layer is mathematically expressed in Equation (2).

$$s_k = \sum_{i=1}^{N} e_k^i x_k^i \tag{2}$$

In Equation (2), s_k is the sum of input data with featured attention weights at time step k. The output is computed based on a softmax function, as expressed in Equation (3).

$$\begin{cases} y_k = softmax(s_k + b_k) \\ softmax(z_i) = \dfrac{e_k^{z_i}}{\sum_{i=1}^{N} e_k^{z_i}} \end{cases} \tag{3}$$

In Equation (3), y_k is the output, b_k is the bias vector, and z_i is the output value at the ith iteration. The softmax function maps multiple neurons' outputs to the probability distribution of intervals (0, 1) with a sum of 1, which is used by the dense layer.

2.2 *Stochastic weight algorithm for the DFFNN*

As a deep learning neural network with one-directional processing, DFFNN has been widely used in various applications and research fields. The schematic mathematical representation for the DFFNN is expressed, as shown in Equation (4).

$$f\ (x) = \sum_{i=1}^{n} y_i\ \sigma(w_i^n \cdot x + b_i) \tag{4}$$

In Equation (4), the input $x = [x_1, x_2, x_3, \dots, x_n]^T \in R^n$. The input weights $wi = [w_{i1}, w_{i2}, w_{i3}, \dots, w_{in}] \in R^n$ and the output weights $y_i \in R$ connected to the ith hidden and output nodes, respectively. N is the number of hidden nodes; $b_i \in R$ is the bias vector; $\sigma(\cdot)$ is the hyperbolic tangent function used to scale the input data between [-1, 1] because the target uses both positive and negative values, which is expressed in Equation (5).

$$\sigma\ (x) = \frac{1}{1 + e^{-x}} \tag{5}$$

In Equation (5), e is the network error. Therefore, using a number of data for the training, $u = \{(x_j,\ t_j) :\ x_j \in R^n, x_j \in R, j = 1, 2, 3, \dots, M\}$, which satisfies the expression for the output of the hidden layer $Hy = T$, as shown in Equation (6).

$$H = \begin{bmatrix} \sigma(w_1^n \cdot x_1 + b_1) & \cdots & \sigma(w_n^n \cdot x_1 + b_n) \\ \vdots & \ddots & \vdots \\ \sigma(w_1^n \cdot x_M + b_1) & \cdots & \sigma(w_n^n \cdot x_M + b_n) \end{bmatrix} \quad (6)$$

In Equation (6), H is the matrix of the hidden layer, which is multiplied by the output weights $y = [y_1, y_2, y_3, \dots, y_M]^T$ to obtain the target vectors, $Z = [z_1, z_2, z_3, \dots, z_M]^T$.

Using the stochastic weight algorithm, the weights and biases are uniformly distributed randomly, as $w_i \sim U(w_{min}, w_{max})$ and $b_i \sim U(b_{min}, b_{max})$, respectively, for the DFFNN to overcome overfitting and improve its transfer learning ability. The output weights can be calculated mathematically using the least-squares method with an L2 regularization for computation optimization, as shown in Equation (7).

$$\begin{cases} min(y \in R^N)\{\|Hy - Z\|_2^2\} \\ min(y \in R^N)\{\|Hy - Z\|_2^2 + \alpha\|y\|_2^2\} \end{cases} \quad (7)$$

In Equation (7), α is the regularization factor, which is greater than 0. If α is given such that $H^T H + \alpha I$ is a nonsingular matrix, the minimizer in Equation (7) is then described, as shown in Equation (8).

$$y = H^T Z (H^T H + \alpha I)^{-1} \quad (8)$$

In Equation (8), I denotes the identity matrix.

For long-term dependency problems using large-scale data, the proposed stochastic weight added to the DFFNN (Figure 1 (a and b)) randomly decomposes the feature-extracted input data by the relevant attention mechanism into M dimensions, $u = \{u_1, u_2, u_3, \dots, s_M\}$. For each subset s_i, the corresponding sub-model is derived and initialized with the same input weights and biases. The output matrix of the hidden layer H_{si}, which is a positive definiteness matrix calculated, as shown in Equation (9).

$$\begin{cases} f_s(y) = \dfrac{1}{M}\displaystyle\sum_{i=1}^{M} f_{si}(y) \\ f_{si}(y) = \dfrac{1}{2}\|H_{si}y - Z_{si}\|_2^2 \end{cases} \quad (9)$$

In Equation (9), $i = 1, 2, 3, \dots, M$, which represents the network's hidden output matrix and target output. Calculate the optimal range of input weights and biases based on the activation function, as shown in Equation (10).

$$\begin{cases} w_i \in \left[\ln\left(\frac{1-r}{r}\right), u \cdot \ln\left(\frac{1-r}{r}\right)\right] \\ b_i \in \begin{cases} [0, w_i], w_i \leq 0 \\ [-w_i, 0], w_i > 0 \end{cases} \end{cases} \tag{10}$$

Therefore, when establishing the output weight, randomly initialize the output matrix as $y(0)$ and compute the local and global gradients, as shown in Equation (11).

$$\begin{cases} \nabla f_{si}(y_k) = H_{si}^T(H_{si}y_{k-1} - Z_{si}) \\ \nabla f_s(y_k) = \frac{1}{M}\sum_{i=1}^{M} \nabla f_{si}(y_k) = \frac{1}{M}\sum_{i=1}^{M} H_{si}^T(H_{si}y_{k-1} - Z_{si}) \\ \nabla^2 f_{si}(y_k) = H_{si}^T H_{si} \end{cases} \tag{11}$$

In this instance, each local neuron is locally optimized throughout each iteration, as shown in Equation (12).

$$y_k = argmin(y)\left[f_{si}(y_{k-1}) - \left(\nabla f_{si}(y_{k-1}) - \rho\nabla f_s(y_{k-1})\right)^T y + \frac{\alpha}{2}\|y_k - y_{k-1}\|_2^2\right] \tag{12}$$

To further understand this local network, the concept of Bregman divergence is presented, as shown in Equation (13).

$$D_\varphi(y_k, \hat{y}_k) = \varphi(y_k) - \varphi(\hat{y}_k) - \nabla\varphi(\hat{y}_k) \cdot (y_k - \hat{y}_k) \tag{13}$$

In the algorithm, each sub-model $f_{si}(y)$, has a complete computation, as shown in Equation (14).

$$F_i(\hat{y}_k) = f_{si}(y) + \frac{\alpha}{2}\|\hat{y}_k\|_2^2 \tag{14}$$

If the regularization parameter α is greater than 0, the Bregman divergence is accordingly, as shown in Equation (15).

$$D_i(y_k, \hat{y}_k) = D_{fi}(y_k, \hat{y}_k) = D_{f_{si}}(y_k, \hat{y}_k) + \frac{\alpha}{2}\|y_k - y_{k-1}\|_2^2 \tag{15}$$

Based on Equations (13) to (15), Equation (12) is transformed to obtain Equation (16).

$$y_k = argmin(y)\left[f_s(y_{k-1}) - \nabla f_s(y_{k-1}) \cdot (y_k - y_{k-1}) + \frac{1}{\mu}D_i(y_k - y_{k-1})\right] \tag{16}$$

Therefore, using the Taylor series expansion, the Bregman divergence is transformed, as shown in Equation (17).

$$D_i(y_k, \hat{y}_k) = y_{k-1} - \alpha(\nabla^2 f_{si}(y_k) + \mu I)^{-1} \cdot \nabla f_s(y_{k-1}) \tag{17}$$

The final optimized output values by the stochastic weight algorithm for the DFFNN are computed based on the aforementioned derivations to obtain Equation (18).

$$\hat{y}_k = y_{k-1} - \alpha\left(\frac{1}{M}\sum_{i=1}^{M}(\nabla^2 f_{si}(y_k) + \mu I)^{-1}\right) \cdot \nabla f_s(y_{k-1}) \tag{18}$$

Using the enhanced feature extraction inputs, the proposed stochastic weight algorithm decomposes the feature-extracted samples into M equal sub-model sample points. All samples are normalized to assess the network's efficacy. The overall architecture of the proposed stochastic weight algorithm and the DFFNN are presented in Figure 1.

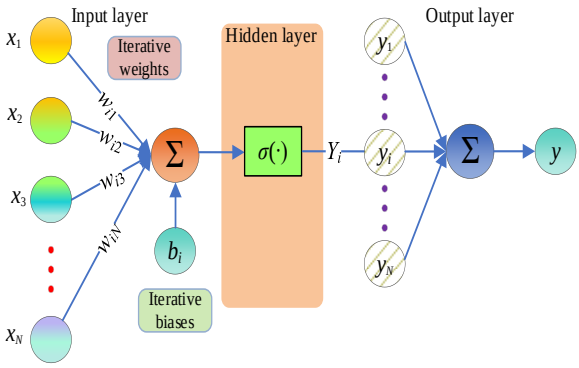

(a) Modeling architecture of the stochastic weight algorithm: $x_i = [I_i, V_i]$

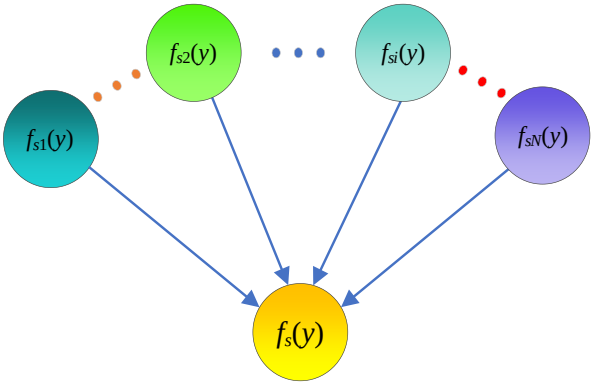

(b) Internal decomposed architecture and principle: The connection between the local neuron $f_{si}(y)$ and the global neuron $f_s(y)$

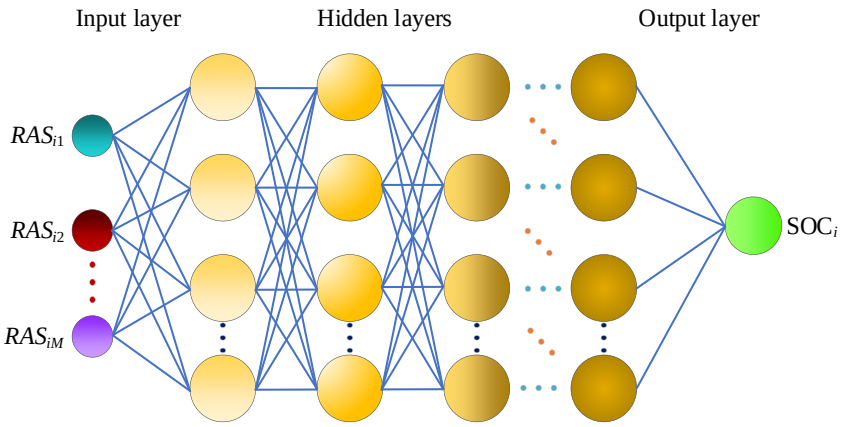

(c) The architecture of the DFFNN

Figure 1. The overall architecture of the proposed stochastic weight algorithm and DFFNN

From Figure 1 (a), the stochastic weight algorithm for DFFNN provides the convergence of the output weights of the unified learning model by breaking the entire feature-extracted training sample into numerous tiny subsets and using each subset to produce a local learning model to incorporate the uniform classifier. During the estimation, the parameter $r = 0.2 - 0.5$ for the stochastic weight algorithm to adaptively calculate the input weights and biases. The number of subsets $u = 10 - 20$, which is based on the dimension of the original input data. Additionally, take the regularization parameter $\mu = 0.03$, and a threshold value of 10^{-3}.

2.3 *Training procedure and hyperparameter selection*

To ensure an estimation with minimized noise and optimal accuracy and performance, the DFFNN is trained using a mini-batch size dependent on each network's adaptability and the quantity of available hardware memory. To avoid overfitting, conventional approaches include retraining the network with more or fewer layers and neurons, as well as adding a dropout layer with a specific dropout probability. Moreover, the dropout layer promotes the generalization ability by dropping the neurons randomly at each layer during training, resulting in less sensitivity of the network to the specific weights of neurons [61]. The overall trial-and-error process of neural network models for lithium-ion battery SOC estimation makes them less desirable, especially when the results are also difficult to explain.

A methodology used in training the neural network is the use of a stochastic optimizer, which is essential in searching for convergence based on the hyperparameter selected during the training because employing the appropriate optimizer gives the network higher performance [62]. The adaptive moment estimate optimizer iteratively updates the weights and biases of the network based on the gradient of the loss function using a gradient descent technique [63]. It has good convergence and efficiently updates the learning rate to guarantee quicker optimization at a minimal computational cost. Its mathematical computation is expressed in Equation (19).

$$\begin{cases} m_g = \nabla J(x^N) \\ m_i = \beta_1 m_{i-1} + (1-\beta_1) g_i^1 \\ v_i = \beta_2 v_{i-1} + (1-\beta_2) g_i^2 \\ \widehat{m}_i = \dfrac{m_i}{1-\beta_1^i} \\ \hat{v}_i = \dfrac{v_i}{1-\beta_2^i} \\ w_i = w_{i-1} - \eta \dfrac{\widehat{m}_i}{\sqrt{\hat{v}_i} + \varepsilon} \end{cases} \tag{19}$$

In Equation (19), m and v are the moving averages, and w represents the model weights. ε is a constant term set as 10^{-8} to ensure a positive denominator. The gradient (β_1) and squared gradient (β_2) decay rates are defined as 0.9 and 0.999, respectively, with an initial learning rate (η) set as 0.01 and a gradient threshold of 1. g_i is the gradient on the current mini-batch, which is calculated to study the training and testing performance of the DFFNN based on the mean square error loss function shown in Equation (20).

$$Loss\ function = \frac{1}{N}\sum_{k=1}^{N}(y_k - \hat{y}_k)^2 \tag{20}$$

In Equation (20), N is the total number of data samples, y_k is the actual SOC, and $\hat{y}_k$ is the estimated SOC by the methods at time step k.

2.4 *Transfer learning mechanism*

In this study, the network is trained, tested, and optimized using MATLAB 2021 on a computer with a CPU speed of 2.50 GHz and an Intel(R) Core (TM) i5-7300HQ. The transfer learning mechanism is a type of network architecture that aims to solve state estimation issues by enhancing the network's generalization ability [51]. To facilitate the quick development of the new network, the transfer learning mechanism of the DFFNN has been widely applied in many fields [39]. As it learns to analyze the input data and establish the underlying regression connection, a pre-trained DFFNN can be utilized as a starting point for a new DFFNN for a long-term dependency task. As a result, a new dataset can be used to finetune some layers of the pre-trained network to create a new network with a new dataset that outperforms constructing a newly constructed DFFNN from scratch. In [64], the transfer learning mechanism is described in detail.

In this context, once the DFFNN has been trained on a single dataset for SOC estimation, it is feasible to use the pre-trained network for multiple battery datasets at different charge-discharge rates and temperatures. The DFFNN can be retrained using a new dataset while a few top-layer parameters are fixed to achieve this. To keep the "learned knowledge", parts of the DFFNN hyperparameters are updated while others remain unchanged. It is worth noting that since the DFFNN directly maps the input current and voltage sequence to estimate the SOC, the results are independent. As a result, the estimations do not require an initial SOC.

Several hyperparameter optimizations and tuning options are available, making it possible to find the ideal combination for each specific time-series prediction. After conducting a series of sensitivity analyses using different epochs, hidden neurons, and mini-batch sizes, the hyperparameter selected for the training of the neural network is presented in Table 1.

Table 1. Hyperparameter selected for the neural network

Hyperparameter	Unit
Hidden neurons	64 per hidden layer
Hidden layers	Variable
Training function	trainlm

Dropout layer	1
Epoch	300
Batch size	256
Batch normalization	ReLU for hidden neurons
Nonlinearity	Sigmoid activation for output layer neurons

2.5 *The auto-recursive SUKF denoising algorithm*

It should be noted that the KF method has been used for smoothing the estimation results from a DFFNN to improve the estimation accuracy [51]. However, it can be observed that the accuracy is not optimal and can be improved. Also, the linear nature of the KF does not guarantee robustness under various nonlinear conditions. The UKF method applies the unscented transform to control the nonlinear update problem of the state and error covariance matrices. Therefore, an adaptive probabilistic updating SUKF method based on a Bayesian transformation with more efficient computation and robustness compared to the nonlinear UKF method is proposed in this paper. The most likely state estimation is thus obtained by adaptively updating the probability of each state at each time step. The working principle of the proposed adaptive probabilistic correcting SUKF method with a shifting-step innovation based on the Bayesian transformation is presented in Figure 2.

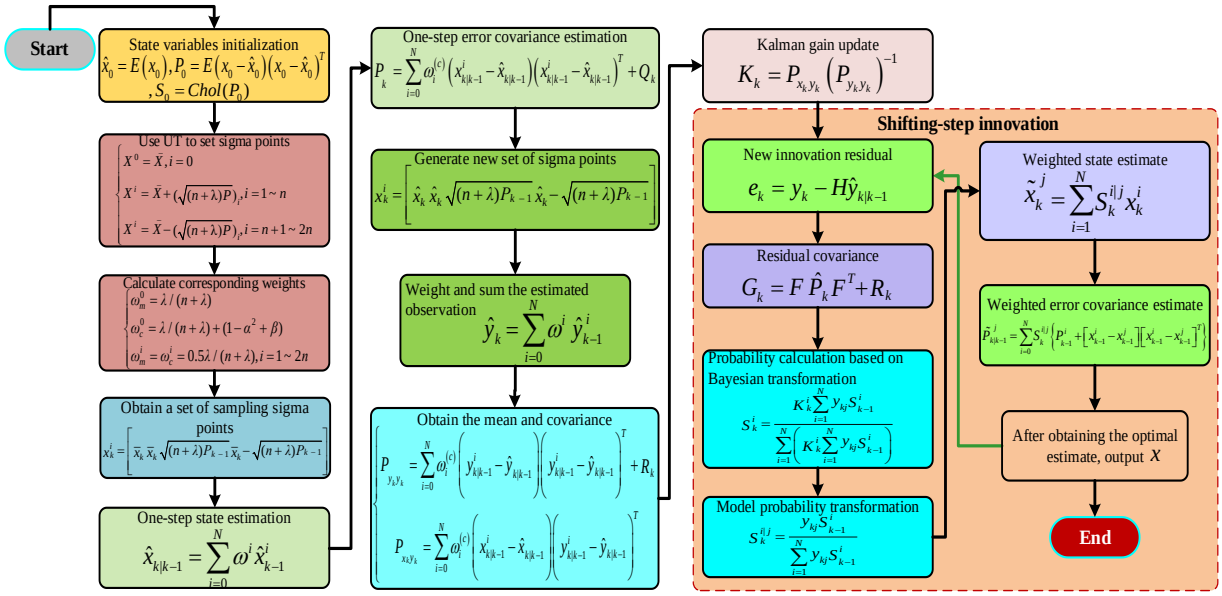

x_k and $\hat{x}_k$ are the priori and posteriori state estimates, respectively, at time step k; P_k and $\hat{P}_k$ are the priori and posteriori error covariance estimates, respectively, at time step k; $\hat{y}$ is the measurement matrix; w_m^i is the mean weight; w_c^i is the error

covariance weight; $\tilde{x}_k^i$ and $\tilde{P}_k^i$ are the posteriori state estimate of featured data i at time step k; $\lambda = \alpha^2\ (n + \kappa) - n$ is the scaling parameter.

Figure 2. The architecture of the SUKF method

As shown in Figure 2, the advantage of the proposed SUKF method is that there is no need to establish a threshold to judge whether the state estimate, error covariance for the uncertainty, and noise covariance quantities are corrected to ensure optimal values. It can determine the state of the battery system during the estimation process, which can adapt to different charge-discharge rates, temperatures, and working conditions.

2.6 *Augmented data description and pre-processing*

Since data pre-processing is significant for accurate SOC estimation by the networks, the current, voltage, and temperature $[I_k, V_k, T_k]$ variables are measured based on real-time working condition tests. Each working conditional-based dataset is normalized before training and testing to improve the robustness and convergence rate of the proposed network and speed up gradient descent. The inputs are normalized within the range of [−1, 1], using the expression in Equation (21).

$$x_n = \frac{2(x - x_{min})}{x_{max} - x_{min}} - 1 \tag{21}$$

In Equation (21), x_n denotes the normalized data, and x denotes the original data. x_{min} and x_{max} are the minimum and maximum values in the dataset, respectively.

To calculate battery SOC mathematically, the voltage and current series are sampled at the kth sampling instant using a window of length w, as shown in Equation (22).

$$y_k = f\big(I(k-w\ +\ 1, k-w+\ 2, k-w\ +\ 3, \ldots, k)\ , V(k-\ w+\ 1, k-\ w+\ 2, k-w+\ 3, \ldots, k)\big), w \leqslant k \leqslant N \tag{22}$$

In Equation (22), $(I(k-\ w\ +\ 1, k-w+\ 2, k-w+\ 3, \ldots, k)$ and $V(k-\ w+\ 1, k-w+\ 2, k-w+\ 3, \ldots, k)$ are the sampled current and voltage series, respectively. y_k is the estimated SOC by the network, $f(\cdot)$ denotes the mapping function of the DFFNN, and N represents the maximum length of the charging period. It is worth noting that the battery's surface temperature is governed by not only the thermal

management system but also the accumulation of the heat generated by the electrochemical reactions, which is measured and directly incorporated into the network as an input to maintain the computational efficiency of the network.

The SOC is defined as the ratio of the remaining energy to the maximum possible energy that the battery can contain, which is one of the crucial functions of the BMS. Its mathematical expression is presented in Equation (23).

$$SOC_k = SOC_0 - \frac{1}{Q_n}\int_0^N \eta I_k dk \tag{23}$$

In Equation (23), SOC_k is the SOC estimated value at time step k. SOC_0 is the SOC value at the initial time step. η is the Coulombic efficiency, which is defined as 1, I_k is the current at time step k, and Q_n is the nominal capacity of the battery.

2.7 *Architectural framework for SOC estimation*

The entire flowchart, which includes the dynamic working states, characteristic battery data, experimental platform design, data pre-processing, and the feature extraction and weight optimization process for SOC estimation, is presented in Figure 3.

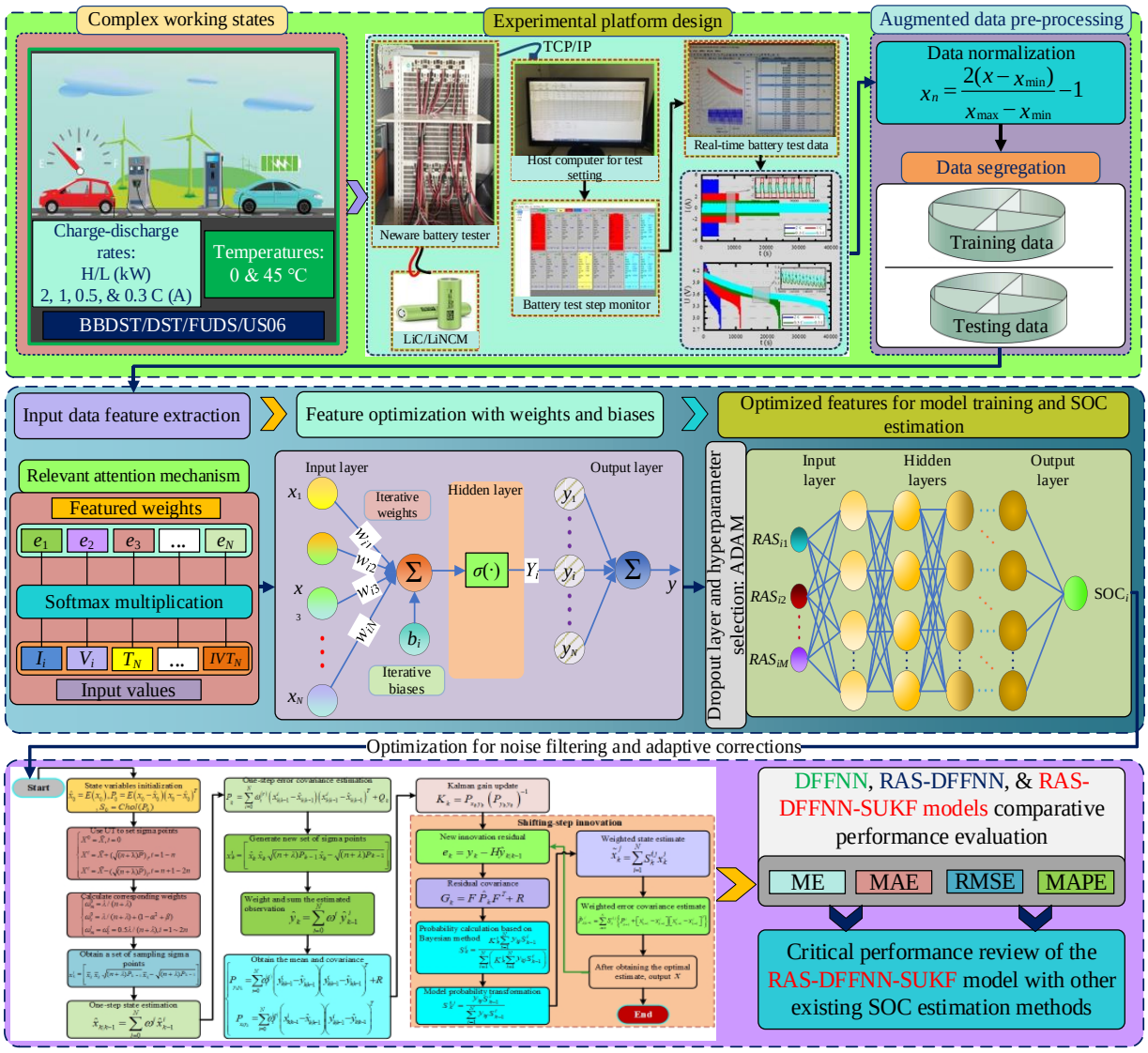

Figure 3. The overview of the proposed models for SOC estimation

In Figure 3, after the SOC is estimated by the DFFNN, RAS-DFFNN, and RAS-DFFNN-SUKF models, a comparative study using the error metrics is conducted to critically evaluate the performance of each model presented in the next section.

2.8 *Performance evaluation criteria*

The maximum error (ME), mean absolute error (MAE), root mean square error (RMSE), and mean absolute percentage error (MAPE) metrics are used, to assess the comparative performance of the proposed method for SOC estimation in this paper, as shown in Equation (24).

$$\begin{cases} E_k = y_k - \hat{y}_k \\ ME = max_k 1,2,\dots,N|E_k| \\ MAE = \dfrac{1}{N}\sum_{k=1}^{N}|E_k| \\ RMSE = \sqrt{\dfrac{1}{N}\sum_{k=1}^{N}(E_k)^2} \\ MAPE = \dfrac{100\%}{N}\sum_{k=1}^{N}\left|\dfrac{E_k}{y_k}\right| \end{cases} \quad (24)$$

In Equation (24), N is the total number of steps in the data sample, and E_k is the estimated SOC error at time step k. y_k is the actual SOC and $\hat{y}_k$ is the SOC estimated at time step k.

3. Experimental battery tests and data collection

In this paper, tests are carried out on an ICR18650-26V lithium cobalt oxide (LiC) battery at different charge-discharge rates under the Beijing bus dynamic stress test (BBDST) and dynamic stress test (DST) at RT (28~32 ℃) conditions. The proposed method is then validated with temperature datasets at 0 and 45 ℃ using an INR18650-20R lithium nickel cobalt manganese oxide (LiNCM) battery under the BBDST, the federal urban driving schedule (FUDS), and US06 working conditions. The technical specifications of the batteries are presented in Table 2.

Table 2. Technical specifications of the batteries

Parameter		LiC	LiNCM
Nominal capacity		2.55 Ah	2.00 Ah
Nominal voltage		3.60 V	3.60 V
Charging	Cut-off voltage	4.20±0.05 V	4.20±0.05 V
	Standard	0.5 C	0.5 C
Discharging	Cut-off voltage	2.5±0.05 V	2.5±0.05 V
	Standard	0.5 C	0.25 C
Chemistry		ICR	INR
Operating temperatures		RT (28~32 ℃)	0 & 45 ℃

LiC (ICR): Higher specific energy density but a higher internal resistance

LiNCM (INR): Hybrid chemistry battery with increased capacity and reduced cost and internal resistance [65, 66]

For the different charge-discharge rates experiment, a Neware battery test equipment (CT-4016-5V100A) is used. Its technical specifications are presented in Table 3.

Table 3. Experimental test equipment specifications for the LiC battery

Cycler manufacturer	Neware battery test equipment
Test channels	16
Current range	0.5~100 A
Charge-discharge voltage range	0.025~5 V
Current/voltage measurement accuracy	±0.1% full scale
Data acquisition rate	0.1 s
Total power	14.2 kW

By switching between CC charging, which prevents overcurrent charging, and CV charging, which prevents overvoltage, per the battery's state, the CC-CV charging strategy promotes longer battery life and increased safety. Using the LiC battery, all the experimental tests on the battery begin with a CC-CV charging strategy, which is applied until the maximum capacity is reached. A 30-minute rest is followed by the discharge steps to ensure electrochemical and thermal equilibrium. Figure 4 shows the characteristics of the real operating charge-discharge rate current and voltage curves at RT for the BBDST and DST working condition experiments.

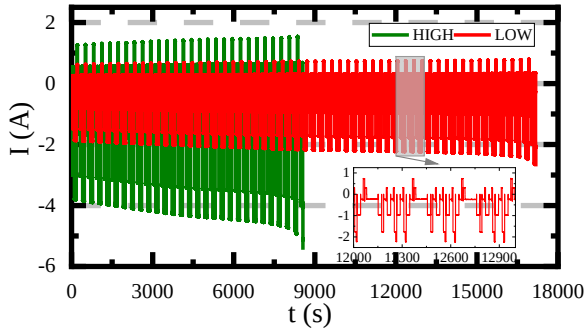

(a) Current curves at low and high-power rates under the BBDST working condition

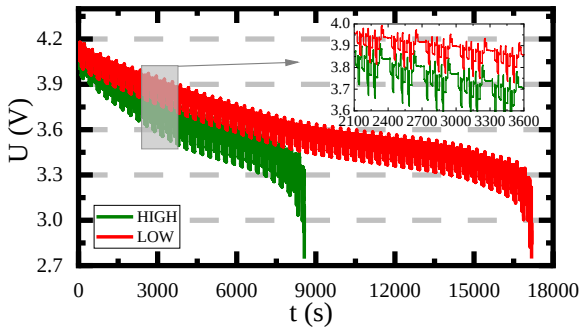

(b) Voltage curves at low and high-power rates under the BBDST working condition

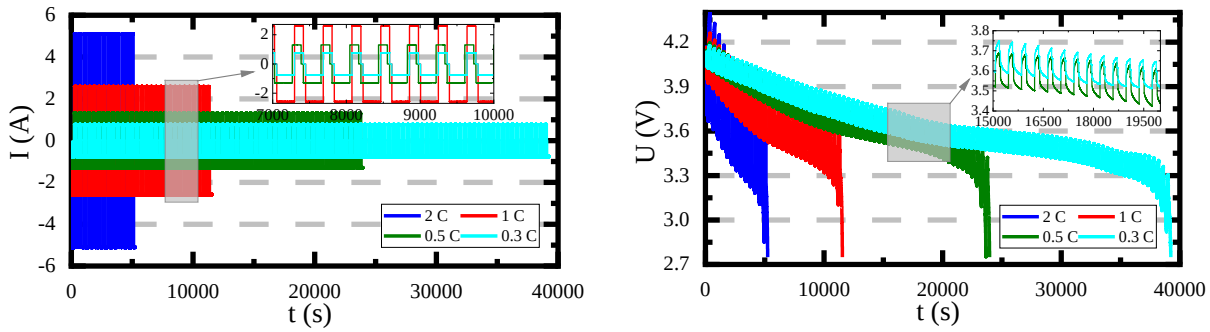

(a) Current curves at 2, 1, 0.5, and 0.3 C under the DST working condition

(b) Voltage curves at 2, 1, 0.5, and 0.3 C under the DST working condition

Figure 4. Charge-discharge rate current and voltage curves under the BBDST and DST working conditions

For the temperature study, the datasets are obtained by applying various driving cycles with standard charge-discharge profiles using a cylindrical LiNCM battery. At the beginning of the test, the cell is subjected to a CC-CV charging strategy. The test temperatures used are 0 and 45 ℃ in tandem under the BBDST, FUDS, and US06 working conditions. More details about the test procedures and the typical current and voltage profiles at various temperatures are given in [56, 67, 68].

4. Results and discussion

In this paper, to test the deep learning, generalization, and transfer learning abilities of the network, a training sequence and computational cost are constructed, as shown in Table 4.

Table 4. Training and testing sequence and cost for the DFFNN and RAS-DFFNN

Working conditions	Training RMSE		Training iteration	
Training	DFFNN	RAS-DFFNN	DFFNN	RAS-DFFNN
BBDST (high)	0.0042159	0.0034835	209500	167950
DST (2 C)	0.0038013	0.0029642	98750	77250
FUDS (0 ℃)	0.0051237	0.0037109	153700	127600
US06 (0 ℃)	0.0043254	0.0033416	141550	112300

Table 4 shows the training sequence and computational cost for the DFFNN and RAS-DFFNN models. For the charge-discharge rate estimation, the high power of the BBDST and the 2 C rate of the DST datasets are used for the training based on the working condition. In addition, because of the small sample size and the number of iterations required to ensure computational efficiency and high accuracy, 0 ℃ datasets are used for training the model in such a way that generalization and transfer learning abilities are exhibited.

4.1 *SOC estimation at different charge-discharge rates and working conditions*

The comparative SOC estimations are carried out using the DFFNN, RAS-DFFNN, and RAS-DFFNN-SUKF models at different charge-discharge rates under the BBDST and DST working conditions.

4.1.1 *SOC estimation results at different charge-discharge rates*

The comparative SOC results for the DFFNN, RAS-DFFNN, and RAS-DFFNN-SUKF models at different charge-discharge rates under the BBDST and DST working conditions are presented in Figure 5. The comparative SOC results at high- and low-power rates under the BBDST working condition are presented in Figure 5 (a).

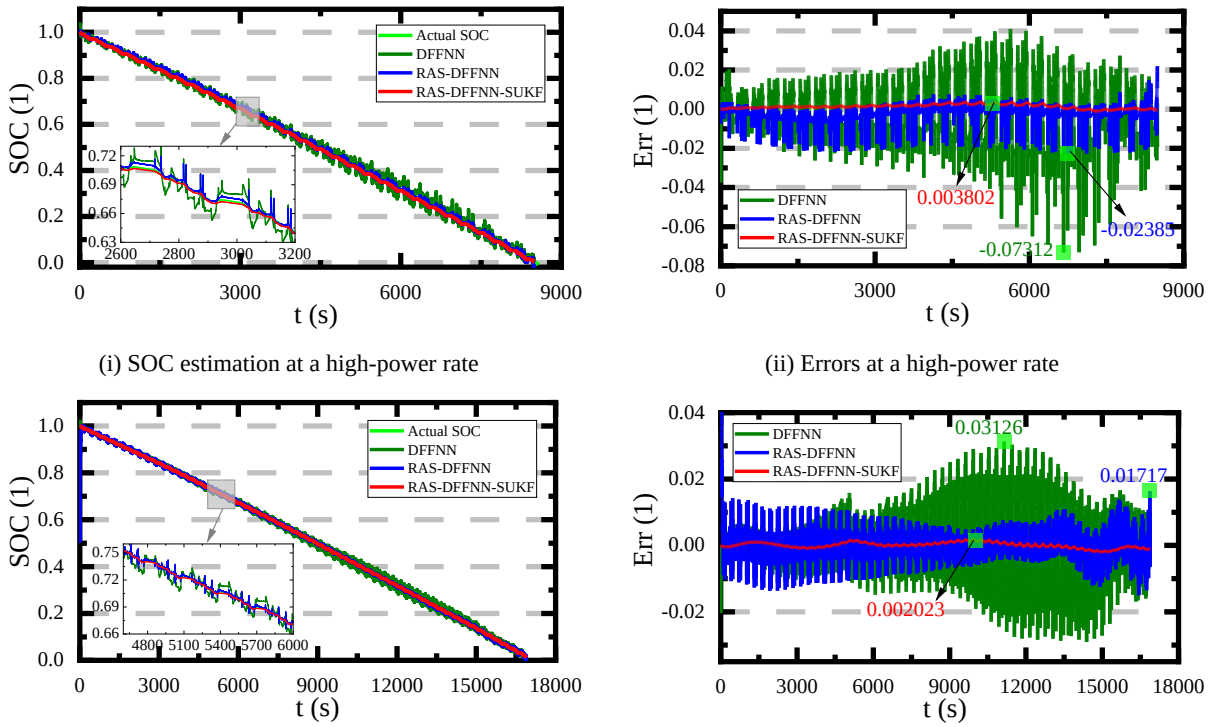

(i) SOC estimation at a high-power rate

(ii) Errors at a high-power rate

(i) SOC estimation at a low-power rate

(ii) Errors at a low-power rate

Figure 5 (a). SOC estimation results at different charge-discharge rates under the BBDST working condition

In Figure 5 (a), it can be observed that the estimation of the DFFNN has more noise compared to the RAS-DFFNN and RAS-DFFNN-SUKF models at high- and low-power rates. At a high power rate, the DFFNN estimates the SOC with an ME value of 7.312%, while the RAS-DFFNN and RAS-DFFNN-SUKF models have ME values of 2.385% and 0.3802%, respectively. Also, at a low power rate, the DFFNN has an ME value of 3.126%, while the RAS-DFFNN and RAS-DFFNN-SUKF models have 1.717% and

0.2023%, respectively. At different charge-discharge power rates, it can be observed that the RAS-DFFNN-SUKF model's performance is optimal because its estimations have less noise and errors, good initialization, and much stability in estimating the SOC of lithium-ion batteries, thanks to its adaptive probabilistic correction feature.

Additionally, the comparative SOC performance for the DFFNN, RAS-DFFNN, and RAS-DFFNN-SUKF models at 2, 1, 0.5, and 0.3 C under the DST working condition are presented in Figure 5 (b).

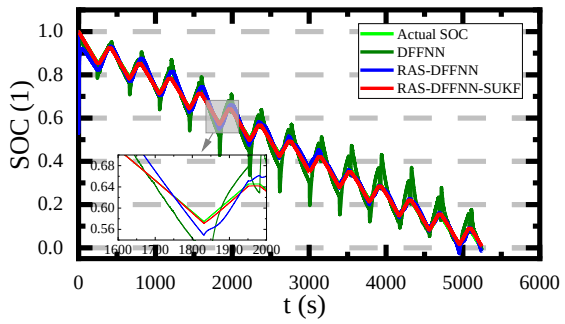

(i) SOC estimation at 2 C

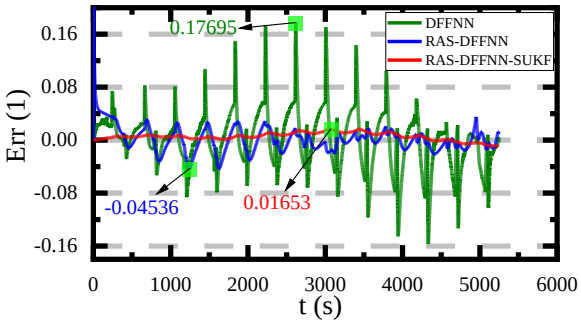

(ii) Errors at 2 C

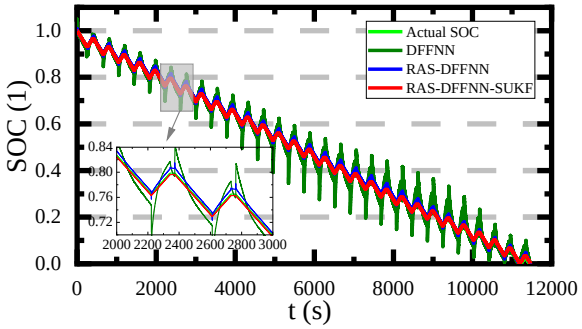

(i) SOC estimation at 1 C

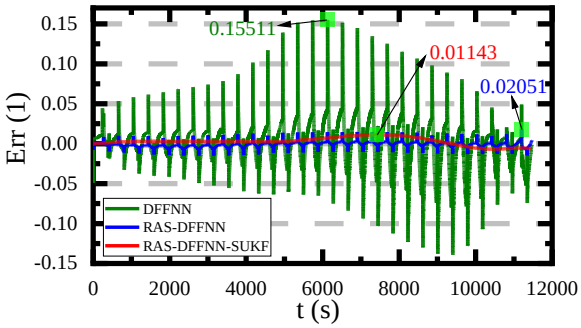

(ii) Errors at 1 C

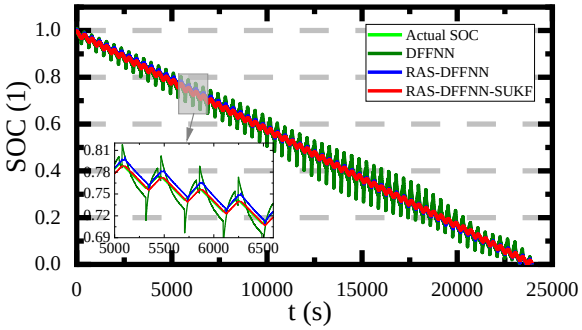

(i) SOC estimation at 0.5 C

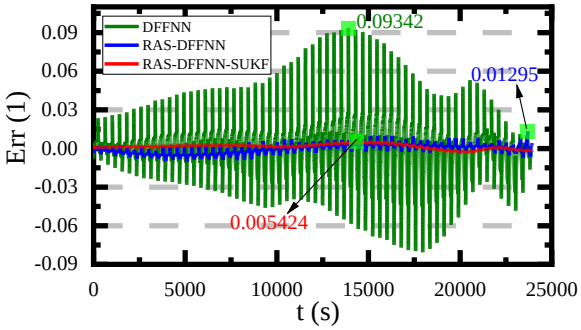

(ii) Errors at 0.5 C

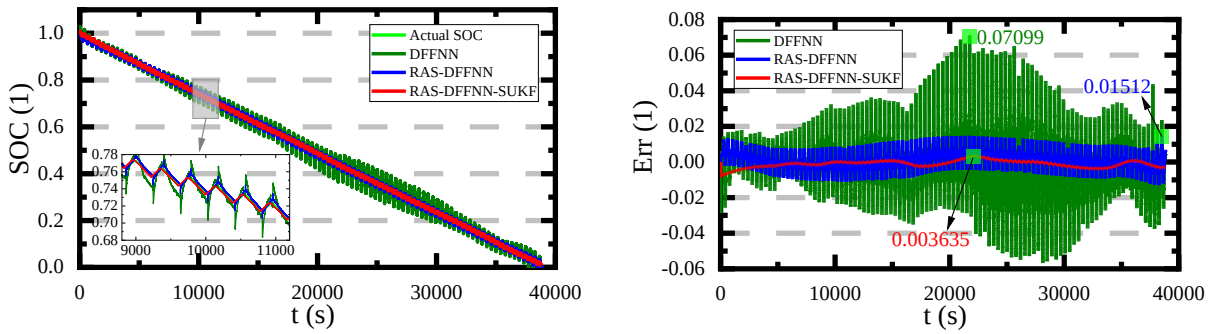

(i) SOC estimation at 0.3 C (ii) Errors at 0.3 C

Figure 5 (b). SOC estimation results at different charge-discharge rates under the DST working condition

In Figure 5 (b), it can also be observed that the estimations by the DFFNN have more noise compared to the RAS-DFFNN and RAS-DFFNN-SUKF models at different current rates under the DST working condition. At 2, 1, 0.5, and 0.3 C, the DFFNN estimates the SOC with ME values of 17.695%, 15.551%, 9.342%, and 7.099%, respectively, which shows a monotonic increasing order with the current rate with high and sparse error spikes compared to decreasing current rates. These outcomes demonstrate the characteristics when the SOC is estimated at low current rates using the DFFNN. Using the RAS-DFFNN model, ME values of 1.653%, 2.051%, 1.295%, and 1.512%, respectively, showing fewer noise and error spikes with improved accuracy. Meanwhile, the results of the RAS-DFFNN-SUKF model are optimal, showing ME values of 1.653%, 1.143%, 0.5424%, and 0.3635%, respectively, at 2, 1, 0.5, and 0.3 C. Furthermore, it has more consistent and optimal performance with less noise and fluctuations for different charge-discharge current rates.

Generally, it can be observed that the RAS-DFFNN-SUKF model has optimal performance compared to that of the DFFNN and RAS-DFFNN at different charge-discharge rates under BBDST and DST working conditions. The results of RAS-DFFNN show to be optimal compared to the DFFNN due to the relevant attention mechanism and stochastic weight algorithm's feature extraction and weight-bias balancing capabilities. However, the final proposed RAS-DFFNN-SUKF model is consistently optimal and accurate to ensure a robust SOC estimation of lithium-ion batteries due to the SUKF method's probabilistic correction of the estimates of the state, error covariance, and noise covariance quantities using its Bayesian transformation.

4.1.2 *Performance evaluation results at different charge-discharge rates*

The MAE, RMSE, and MAPE metrics are used to critically evaluate the performance of the models and examine their ability to accurately estimate the SOC at various charge-discharge rates, as presented in Figure 6.

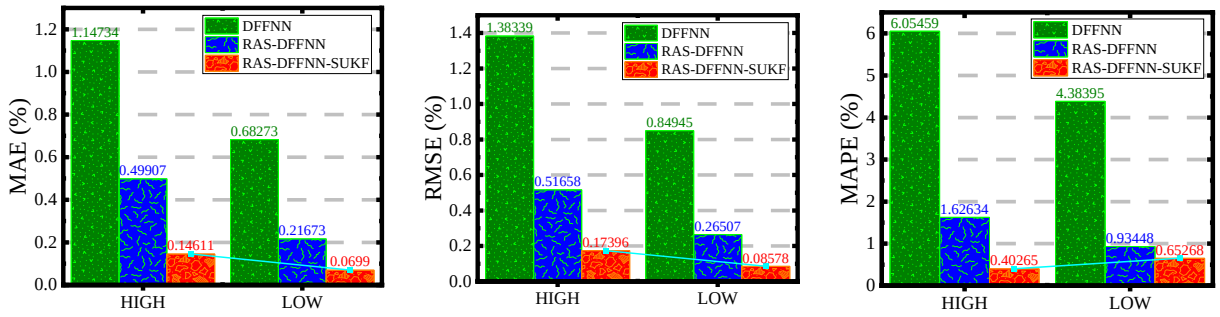

(a) BBDST working condition

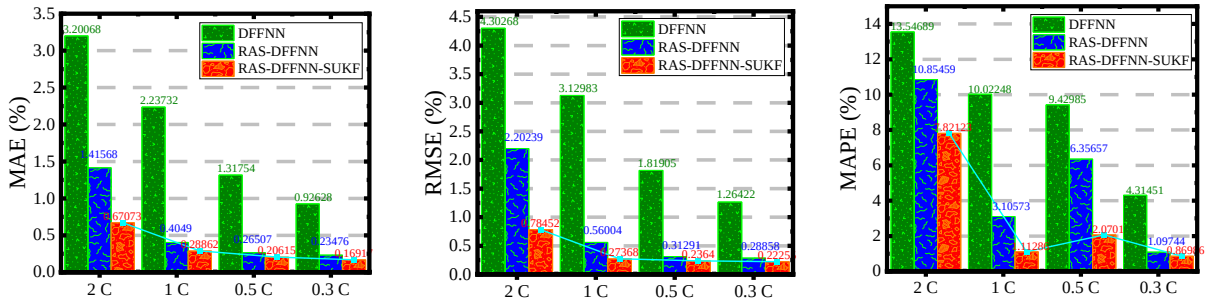

(b) DST working condition

Figure 6. Evaluation of the DFFNN, RAS-DFFNN, and RAS-DFFNN-SUKF models' performance at various charge-discharge rates

Figure 6 presents the critical performance evaluation of the DFFNN, RAS-DFFNN, and RAS-DFFNN-SUKF models at different charge-discharge rates under the BBDST and DST working conditions using the MAE, RMSE, and MAPE metrics.

In Figure 6 (a), at different power rates, it can be observed that the DFFNN has optimal MAE, RMSE, and MAPE values of 0.68273%, 0.84945%, and 4.38395%, respectively, occurring at a low power rate. Also, the RAS-DFFNN is observed to have optimal MAE, RMSE, and MAPE values of 0.21673%, 0.26507%, and 0.93448%, respectively. Meanwhile, the final proposed RAS-DFFNN-SUKF estimates the SOC with the overall best MAE, RMSE, and MAPE values of 0.0699%, 0.08578%, and 0.40265%,

respectively, at different charge-discharge rates, which showed a downtrend for the MAE and RMSE with decreasing power rate and vice versa for the MAPE.

Additionally, in Figure 6 (b), at different current rates, it can be observed that the DFFNN estimates the SOC with results having optimal MAE, RMSE, and MAPE values of 0.92628%, 1.26422%, and 4.31451%, respectively. Then, the RAS-DFFNN respectively has 0.23476%, 0.28858%, and 1.09744%. Meanwhile, the RAS-DFFNN-SUKF model has the overall best MAE, RMSE, and MAPE values of 0.1691%, 0.2225%, and 0.86985%, respectively, at different charge-discharge rates, which also showed a dynamic trend similar to that of the estimations under the DST working condition, verifying its adaptability and robustness under this working condition as well.

These optimal outcomes by the proposed models show consistent performance improvements at various charge-discharge rates and operating conditions, demonstrating their adaptability and robustness in estimating the SOC of lithium-ion batteries. This is due to the relevant attention mechanism, stochastic weight algorithm, and the adaptive probabilistic correction of the state, uncertainty, and noise covariance correction using the SUKF, which has shifting-step innovation based on the Bayesian transformation.

4.2 *SOC estimation at different operating temperatures and working conditions*

The results of the DFFNN, RAS-DFFNN, and RAS-DFFNN-SUKF models' comparative SOC estimation at different temperatures under the BBDST, FUDS, and US06 working conditions are presented in this section.

4.2.1 *SOC estimation results at different operating temperatures*

The comparative SOC performance results of the DFFNN, RAS-DFFNN, and RAS-DFFNN-SUKF models at temperatures of 0 and 45 ℃ under the BBDST, FUDS, and US06 working conditions are presented in Figure 7. The SOC estimation results at different temperatures under the BBDST working condition are presented in Figure 7 (a).

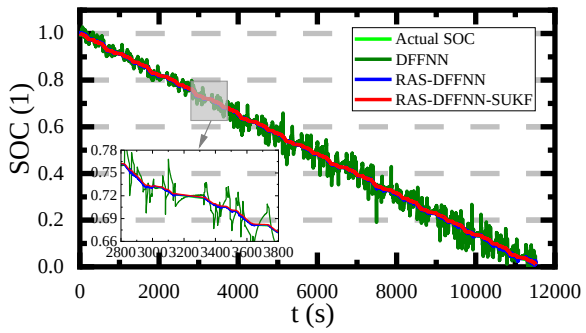

(i) SOC estimation at 0 ℃

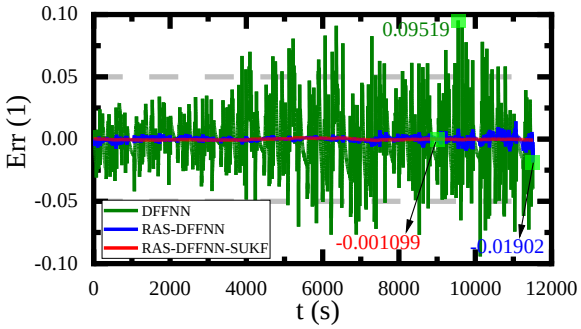

(ii) Errors at 0 ℃

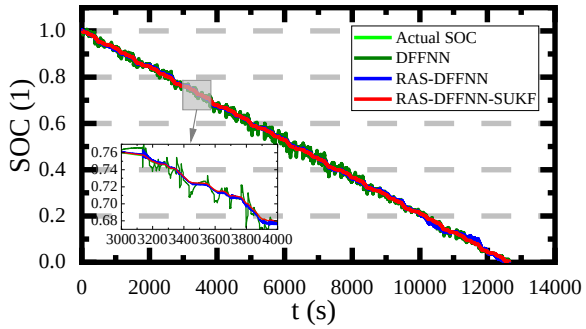

(i) SOC estimation at 45 ℃

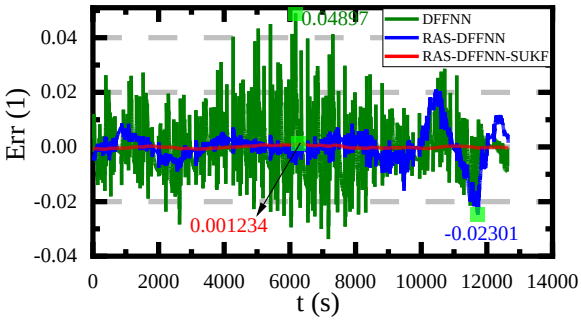

(ii) Errors at 45 ℃

Figure 7 (a). SOC estimation results at different temperatures under the BBDST working condition

In Figure 7 (a), it can be observed that the SOC estimation results for the DFFNN have ME values of 9.519% and 4.897% at temperatures of 0 and 45 ℃, respectively, with high noise effects and fluctuations. Then, the RAS-DFFNN also estimates the SOC with ME values of 1.902% and 2.301% at temperatures of 0 and 45 ℃, respectively. Meanwhile, the SOC results of the RAS-DFFNN model are observed to have more stable, refined, and optimized SOC estimation at both temperatures. At 0 and 45 ℃, it accurately estimates the SOC with ME values of 0.1099% and 0.1234%, respectively. Moreover, the SUKF method stabilizes and eliminates the noise fluctuations in the estimation, especially at 45 ℃, which occurred as a result of the high discharge level.

Additionally, the comparative SOC performance results for the DFFNN, RAS-DFFNN, and RAS-DFFNN-SUKF models at 0 and 45 ℃ under the FUDS working condition are presented in Figure 7 (b).

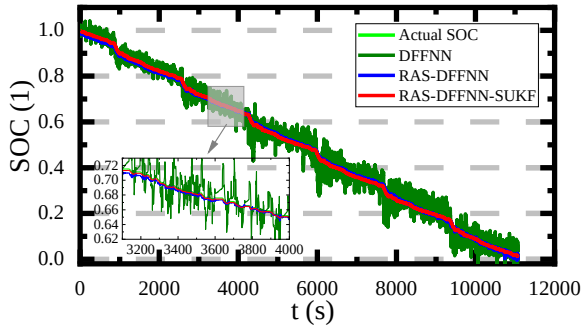

(i) SOC estimation at 0 ℃

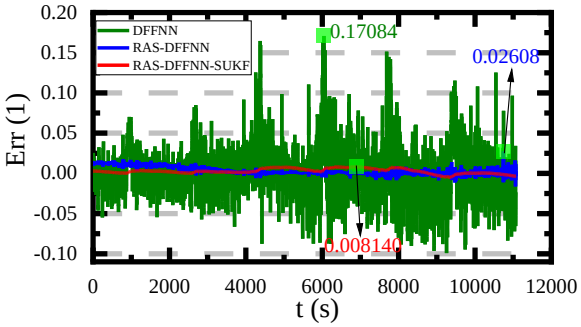

(ii) Errors at 0 ℃

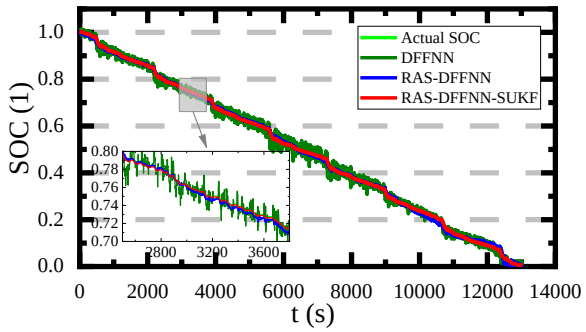

(i) SOC estimation at 45 ℃

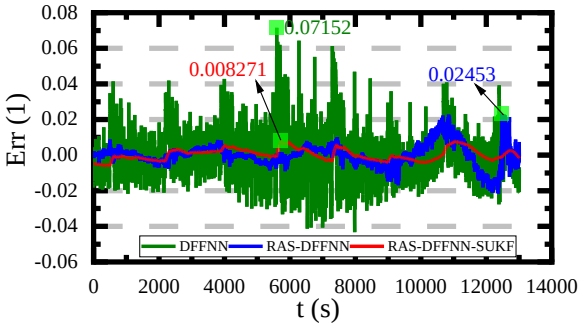

(ii) Errors at 45 ℃

Figure 7 (b). SOC estimation results at different temperatures under the FUDS working condition

In Figure 7 (b), it can be observed that the DFFNN has more noise effects at 0 ℃ compared to the estimation results at 45 ℃. It estimates the SOC with ME values of 17.084% and 7.152%, respectively. Then, the proposed RAS-DFFNN estimates the SOC with ME values of 2.608% and 2.453% at temperatures of 0 and 45 ℃, respectively. Meanwhile, the final proposed RAS-DFFNN-SUKF model estimates the SOC with ME values of 0.8140% and 0.8271% at 0 and 45 ℃, respectively. Furthermore, it can be observed that the estimations at 45 ℃ fluctuate much closer to the end of discharge, but the SUKF does well in smoothing out the fluctuations and noise for optimal estimation results.

Finally, Figure 7 (c) compares the SOC performance results for the DFFNN, RAS-DFFNN, and RAS-DFFNN-SUKF models at 0 and 45 ℃ under the US06 working condition.

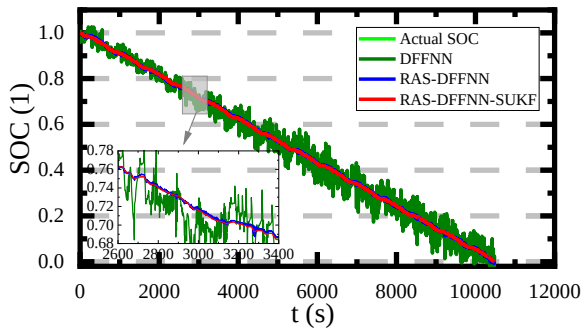

(i) SOC estimation at 0 ℃

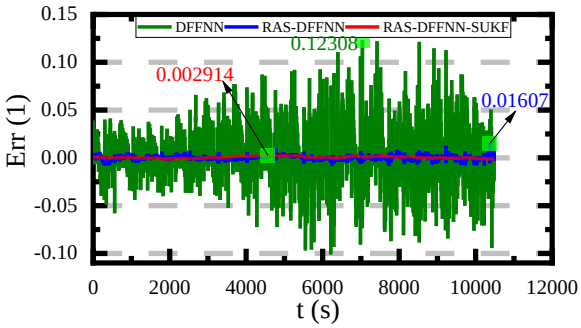

(ii) Errors at 0 ℃

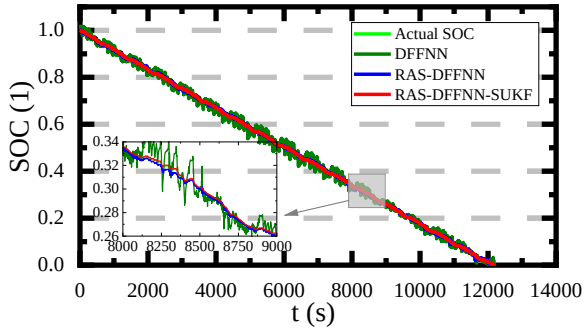

(i) SOC estimation at 45 ℃

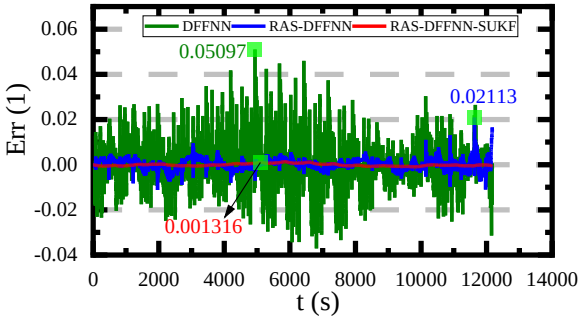

(ii) Errors at 45 ℃

Figure 7 (c). SOC estimation results at different temperatures under the US06 working condition

As presented in Figure 7 (c), it can be observed that the DFFNN also exhibits higher noise effects at 0 ℃ than at 45 ℃ under the US06 working condition. It estimates the SOC with ME values of 12.308% and 5.097%, respectively. Also, the RAS-DFFNN estimates the SOC with ME values of 1.607% and 2.113% at temperatures of 0 and 45 ℃, respectively. Meanwhile, at 0 and 45 ℃, the RAS-DFFNN-SUKF model estimates the SOC with ME values of 0.2914% and 0.1316%, respectively, which are optimal and accurate enough to verify the robustness of the proposed model.

Generally, based on the performance using the error curves, it can be observed that the SOC estimation results achieved by the finally proposed RAS-DFFNN-SUKF model at different temperatures under various working conditions have optimal and noise-less characteristics for online SOC estimation by the BMS for EVs. It is due to the optimal abilities of the proposed relevant attention mechanism, stochastic weight, and the adaptive probabilistic correction SUKF method with a shifting-step innovation based on the Bayesian transformation.

4.2.2 *Performance evaluation results at different operating temperatures*

The critical SOC performance evaluations of the DFFNN, RAS-DFFNN, and RAS-DFFNN-SUKF models at 0 and 45 ℃ under the BBDST, FUDS, and US06 working conditions are presented in Figure 8.

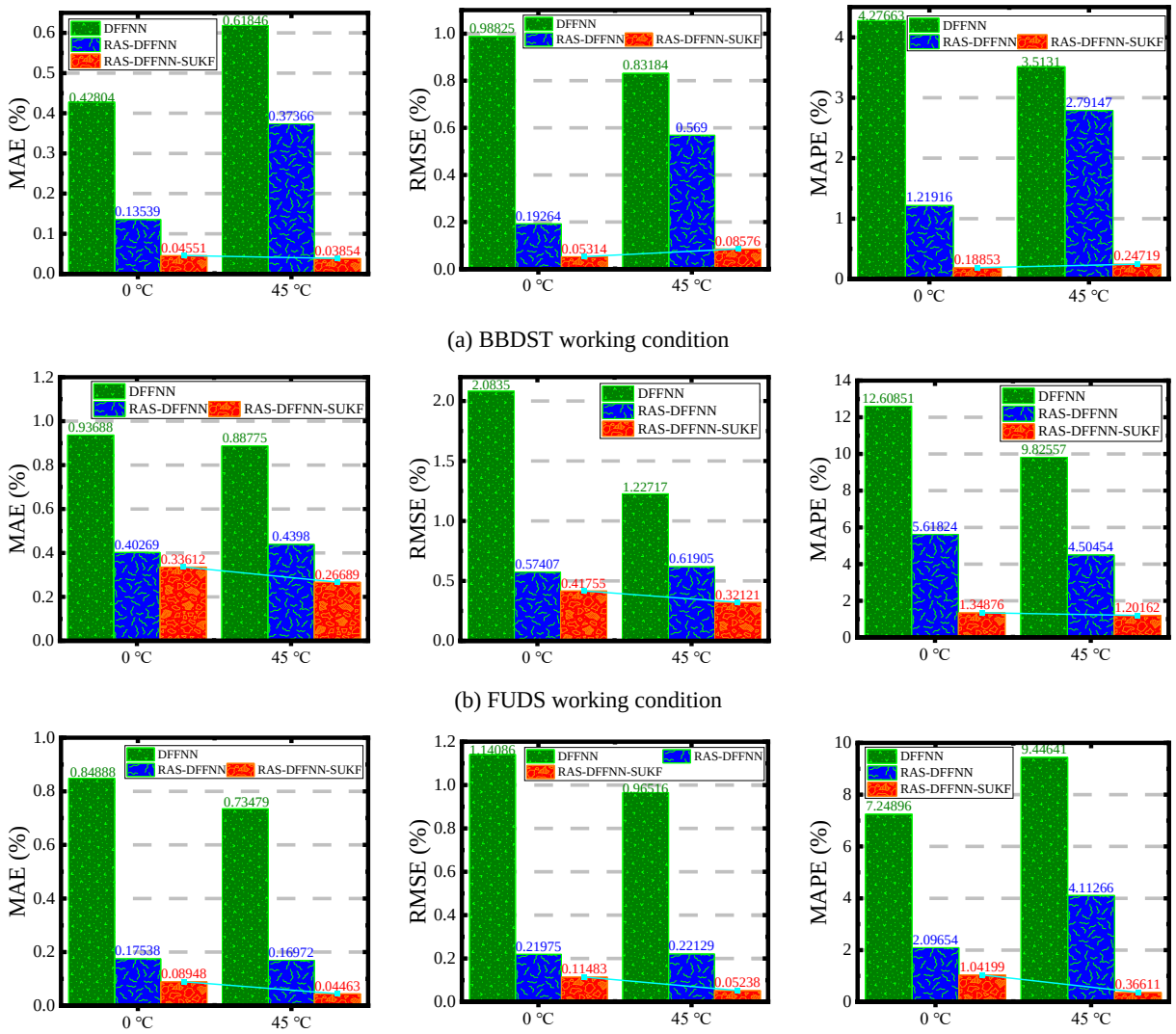

(a) BBDST working condition

(b) FUDS working condition

(c) US06 working condition

Figure 8. Performance evaluation of the DFFNN, RAS-DFFNN, and RAS-DFFNN-SUKF models at different temperatures

In Figure 8, at different temperatures, it can be observed that using the overall best MAE, RMSE, and MAPE values, the DFFNN has the highest error values compared to the RAS-DFFNN and RAS-DFFNN-SUKF models under the BBDST, FUDS, and US06 working conditions.

Under the BBDST working condition, the DFFNN has optimal MAE, RMSE, and MAPE values of 0.42804%, 0.83184%, and 3.5131%, respectively. However, it can be observed that the RAS-DFFNN has

values of 0.31539%, 0.19264%, and 1.21916%, respectively. Meanwhile, the RAS-DFFNN-SUKF model has the overall best MAE, RMSE, and MAPE values of 0.03854%, 0.05314%, and 0.18853%, respectively, which are highly optimal compared to the performances of the previous SOC estimation models at different temperatures.

Furthermore, at 0 and 45 ℃ under the FUDS working condition, it can be observed that the DFFNN estimates the SOC with optimal MAE, RMSE, and MAPE values of 0.88775%, 1.22717%, and 9.82557%, respectively. Then, the RAS-DFFNN has values of 0.40269%, 0.57407%, and 4.50454%, respectively. Meanwhile, the final proposed RAS-DFFNN-SUKF model has the overall best MAE, RMSE, and MAPE values of 0.26689%, 0.32121%, and 1.02162%, respectively.

Finally, under the US06 working condition, it can also be observed that the DFFNN estimates the SOC with optimal MAE, RMSE, and MAPE values of 0.73479%, 0.96516%, and 7.24896%, respectively, at temperatures of 0 and 45 ℃. Also, the RAS-DFFNN has, respectively, 0.16972%, 0.21975%, and 2.09654%. The final proposed RAS-DFFNN-SUKF model has the overall best MAE, RMSE, and MAPE values overall, with values of 0.04463%, 0.05238%, and 0.36611%, respectively.

Generally, it can be observed that the performance of the RAS-DFFNN-SUKF model outperforms the DFFNN and RAS-DFFNN with significant improvements to ensure an accurate online SOC estimation of lithium-ion batteries under various temperatures and complex working conditions. Furthermore, it can also be used to estimate the SOC of batteries with different chemistries and significantly reduces the laborious and time-intensive process of other estimation methods. However, the RAS-DFFNN model architecture will remain the same if it is used to perform SOC estimation on different batteries by simply using its transfer learning capabilities to retrain the last few layers of the network. This would take less time than parameterizing a model for a different battery, as is usually done for conventional networks.

4.3 *Comparison of the proposed RAS-DFFNN-SUKF model with other existing SOC methods*

Additionally, a critical comparative study is conducted for the RAS-DFFNN-SUKF model, verifying its superiority over other existing methods, as presented in Table 5.

Table 5. Critical performance review of the RAS-DFFNN-SUKF model with other existing SOC methods

Methods	Battery	Verification conditions	Specifications	Lowest metric values
GRU-TL [56]	LiNCM3.0Ah	Operating temperatures	32 to 50 ℃	MAE = 0.853%
		Dynamic conditions	FUDS, US06, & UDDS	RMSE = 1.115%
CDTL [58]	LFP1.1Ah	Operating temperature	30 ℃	MAE = 0.48%
		Dynamic condition	FUDS	RMSE = 0.70%
SSMPI [59]	LiNCM2Ah	Operating temperatures	0 to 45 ℃	MAE = 0.664%
		Dynamic conditions	DST, FUDS, US06, & UDDS	
DNN [63]	LiNC2.9Ah	Operating temperatures	−20 to 25 ℃	ME = 2.8%
		Dynamic conditions	UDDS, HWFET, LA92, & US06	MAE = 0.61%
				RMSE = 0.78%
CNN-LSTM [69]	LiFP1.1Ah	Operating temperatures	10 to 50 ℃	MAE = 0.52%
		Dynamic conditions	DST, FUDS, & US06	RMSE = 0.64%
AUTOENCOD-LSTM [70]	Li-NCM2Ah	Operating temperatures	0 to 45 ℃	MAE = 0.51%
		Dynamic conditions	DST & FUDS	MSE = 0.52%
				RMSE = 0.72%
DA-TCN [71]	LiNCM (72 kWh/ rated: 350 V)	Operating temperature	25 ℃	MAE = 0.56%
		Dynamic condition	NEVDMCP	MSE = 0.44%
				RMSE = 0.67%
CNN-BWGRU [72]	LiNCM3Ah	Operating temperatures	−20 to 0 ℃	MAE = 1.04%
		Dynamic conditions	US06 & UDDS	RMSE = 1.37%
				R^2 = 99.76%
Proposed RAS-DFFNN-SUKF	LiC2.55Ah & LiNCM2.00Ah	Operating temperatures	0 to 45 ℃	MAE = 0.03854%
		Charge-discharge rates	High-low power, 2, 1, 0.5, & 0.3 C	RMSE = 0.05238%
		Dynamic conditions	BBDST, DST, FUDS, & US06	MAPE = 0.18853%

Gated recurrent unit with transfer learning (GRU-TL); Deep neural network (DNN); Dual attention-temporal convolutional network (DA-TCN); Convolutional neural network-bidirectional weighted gated recurrent unit (CNN-BWGRU); Urban dynamometer driving schedule (UDDS); Highway fuel economy driving schedule (HWFET); Unified driving schedule (LA92); Supplemental federal test procedures or US06; New energy vehicle data monitoring cloud platform (NEVDMCP); Lithium iron phosphate (LFP)

In Table 5, a comparative analysis is conducted with some existing methods commonly used to estimate the SOC of lithium-ion batteries. According to the overall analysis, the RAS-DFFNN-SUKF model provides the best estimation result with the lowest error metric values, with MAE, RMSE, and MAPE values of 0.03854%, 0.05238%, and 0.18853%, respectively. It is followed by the AUTOENCOD-LSTM, which also has MAE, RMSE, and MAPE values of 0.51%, 0.52%, and 0.72%, respectively. Moreover,

testing and verifying the proposed RAS-DFFNN-SUKF model at various charge-discharge rates and temperatures under various dynamic working conditions using batteries with different chemistries reveals its superiority and robustness compared to the existing methods for SOC estimation of lithium-ion batteries.

5. Conclusion and future work

In this paper, a RAS-DFFNN-SUKF model with a transfer learning mechanism is established for SOC estimation of lithium-ion batteries. In this framework, first, the DFFNN is used to approximate the mapping of battery states using real-time operating condition tests at different charge-discharge rates and temperatures under four working conditions using two different battery chemistries. The proposed RAS algorithm with feature extraction capabilities combines a relevant attention mechanism with stochastic weight optimizations for the DFFNN and solves the gradient problem to estimate the SOC of lithium-ion batteries with enhanced generalization ability. Then, a SUKF method is also proposed to accurately estimate the state, error covariance, and noise covariance quantities of the battery by adaptively correcting the probability of each state with a shifting-step innovation based on the Bayesian transformation to maintain robustness against spontaneous error noise and spikes. According to the validation results, using the transfer learning mechanism, it quickly constructs new DFFNNs with a reliable performance by tuning just one dense layer, and by adding more layers, it can establish DFFNNs with greater accuracy than a newly established neural network. At different charge-discharge rates, the MAE, RMSE, and MAPE results show that the final proposed RAS-DFFNN-SUKF estimates the SOC with the overall best values of 0.0699%, 0.08578%, and 0.40265%, respectively, under the complex BBDST and DST working conditions using the LiC battery. Also, at temperatures of 0 and 45 ℃, it outperforms the previous estimation models by estimating the SOC with the overall best MAE, RMSE, and MAPE values of 0.03854%, 0.05238%, and 0.18853%, respectively, under the complex BBDST, FUDS, and US06 working conditions using the LiNCM battery. These results demonstrate the effectiveness, reliability, and robustness of the proposed RAS-DFFNN-SUKF model for real-time BMS applications in EVs when compared to other existing methods.

Even though the proposed model showed several advantages, our future work will focus on eliminating some of the parameters of the RAS algorithm to give it a simple structure while improving its effectiveness. Then, we will further verify the effectiveness of the proposed RAS-DFFNN-SUKF model for state-of-health estimation, experiments using different charge-discharge rates at subzero temperatures and battery chemistries with higher capacities will be conducted due to the laboratory settings and time constraints.

Declaration of competing interest

The authors declare no known competing financial interests or personal relationships that influence the work reported in this paper.

CRediT authorship statement

Paul Takyi-Aninakwa: Methodology, conceptualization, software, writing-original draft, analysis, and data curation; **Shunli Wang**: Supervision and resources; **Hongying Zhang**: Resources and investigation; **Yang Xiao**: Writing; **Carlos Fernandez**: Writing.

Acknowledgment

The work is supported by the National Natural Science Foundation of China (No. 62173281 and 61801407).

References

1. Song, L., et al., *Intelligent state of health estimation for lithium-ion battery pack based on big data analysis.* Journal of Energy Storage, 2020. **32**.
2. Tran, M.-K., et al., *A comprehensive equivalent circuit model for lithium-ion batteries, incorporating the effects of state of health, state of charge, and temperature on model parameters.* Journal of Energy Storage, 2021. **43**.
3. Zheng, F., et al., *Influence of different open circuit voltage tests on state of charge online estimation for lithium-ion batteries.* Applied Energy, 2016. **183**: p. 513-525.
4. Nian, P., Z. Shuzhi, and Z. Xiongwen, *Co-estimation for capacity and state of charge for lithium-ion batteries using improved adaptive extended Kalman filter.* Journal of Energy Storage, 2021. **40**.
5. Hannan, M.A., et al., *A review of lithium-ion battery state of charge estimation and management system in electric vehicle applications: Challenges and recommendations.* Renewable and Sustainable Energy Reviews, 2017. **78**: p. 834-854.
6. Jibhkate, U.N. and U.B. Mujumdar, *Development of low complexity open circuit voltage model for state of charge estimation with novel curve modification technique.* Electrochimica Acta, 2022. **429**.

7. Zhang, G., B. Xia, and J. Wang, *Intelligent state of charge estimation of lithium-ion batteries based on L-M optimized back-propagation neural network.* Journal of Energy Storage, 2021. **44**.
8. Wang, Y., M. Li, and Z. Chen, *Experimental study of fractional-order models for lithium-ion battery and ultra-capacitor: Modeling, system identification, and validation.* Applied Energy, 2020. **278**.
9. Wang, Y., et al., *A review of key issues for control and management in battery and ultra-capacitor hybrid energy storage systems.* eTransportation, 2020. **4**.
10. Li, W., et al., *Digital twin for battery systems: Cloud battery management system with online state-of-charge and state-of-health estimation.* Journal of Energy Storage, 2020. **30**.
11. Ni, Z., X. Xiu, and Y. Yang, *Towards efficient state of charge estimation of lithium-ion batteries using canonical correlation analysis.* Energy, 2022. **254**.
12. Espedal, I.B., et al., *Current Trends for State-of-Charge (SoC) Estimation in Lithium-Ion Battery Electric Vehicles.* Energies, 2021. **14**(11).
13. Zhang, S. and X. Zhang, *A multi time-scale framework for state-of-charge and capacity estimation of lithium-ion battery under optimal operating temperature range.* Journal of Energy Storage, 2021. **35**.
14. Wang, Y. and Z. Chen, *A framework for state-of-charge and remaining discharge time prediction using unscented particle filter.* Applied Energy, 2020. **260**.
15. Hu, X., et al., *State estimation for advanced battery management: Key challenges and future trends.* Renewable and Sustainable Energy Reviews, 2019. **114**.
16. Tian, J., et al., *Battery state-of-charge estimation amid dynamic usage with physics-informed deep learning.* Energy Storage Materials, 2022. **50**: p. 718-729.
17. Jiang, S. and Z. Song, *Estimating the State of Health of Lithium-Ion Batteries with a High Discharge Rate through Impedance.* Energies, 2021. **14**(16).
18. Duan, W., et al., *An Improved Gated Recurrent Unit Network Model for State-of-Charge Estimation of Lithium-Ion Battery.* Energies, 2020. **13**(23).
19. Wang, S., et al., *A novel feedback correction-adaptive Kalman filtering method for the whole-life-cycle state of charge and closed-circuit voltage prediction of lithium-ion batteries based on the second-order electrical equivalent circuit model.* International Journal of Electrical Power & Energy Systems, 2022. **139**.
20. Wang, Y., et al., *Estimation of battery open-circuit voltage and state of charge based on dynamic matrix control - extended Kalman filter algorithm.* Journal of Energy Storage, 2022. **52**.
21. Mc Carthy, K., et al., *Electrochemical impedance correlation analysis for the estimation of Li-ion battery state of charge, state of health and internal temperature.* Journal of Energy Storage, 2022. **50**.
22. Esser, M., G. Rohde, and C. Rehtanz, *Electrochemical Impedance Spectroscopy Setup based on Standard Measurement Equipment.* Journal of Power Sources, 2022. **544**.
23. Yu, P., et al., *Study of hysteresis voltage state dependence in lithium-ion battery and a novel asymmetric hysteresis modeling.* Journal of Energy Storage, 2022. **51**.
24. Gao, Y., et al., *Enhanced state-of-charge estimation of LiFePO4 batteries using an augmented physics-based model.* Journal of Power Sources, 2022. **544**.
25. Jiang, B., et al., *Joint estimation of lithium-ion battery state of charge and capacity within an adaptive variable multi-timescale framework considering current measurement offset.* Applied Energy, 2019. **253**.
26. Takyi-Aninakwa, P., et al., *A strong tracking adaptive fading-extended Kalman filter for the state of charge estimation of lithium-ion batteries.* International Journal of Energy Research, 2022.
27. He, W., et al., *A Physics-Based Electrochemical Model for Lithium-Ion Battery State-of-Charge Estimation Solved by an Optimised Projection-Based Method and Moving-Window Filtering.* Energies, 2018. **11**(8).
28. Li, J., et al., *A method for SOC estimation based on simplified mechanistic model for LiFePO4 battery.* Energy, 2016. **114**: p. 1266-1276.

29. Cui, Z., et al., *An extended Kalman filter based SOC estimation method for Li-ion battery.* Energy Reports, 2022. **8**: p. 81-87.
30. Xu, C., et al., *Dual fuzzy-based adaptive extended Kalman filter for state of charge estimation of liquid metal battery.* Applied Energy, 2022. **327**.
31. Ouyang, Q., et al., *Adaptive Square-Root Unscented Kalman Filter-Based State-of-Charge Estimation for Lithium-Ion Batteries with Model Parameter Online Identification.* Energies, 2020. **13**(18).
32. Chen, L., et al., *Adaptive state-of-charge estimation of lithium-ion batteries based on square-root unscented Kalman filter.* Energy, 2022. **252**.
33. Liu, M., et al., *A high-order state-of-charge estimation model by cubature particle filter.* Measurement, 2019. **146**: p. 35-42.
34. Zhengxin, J., et al., *An Immune Genetic Extended Kalman Particle Filter approach on state of charge estimation for lithium-ion battery.* Energy, 2021. **230**.
35. Chen, Z., et al., *State-of-charge estimation of lithium-ion batteries based on improved H infinity filter algorithm and its novel equalization method.* Journal of Cleaner Production, 2021. **290**.
36. Chen, Y., et al., *SOC estimation of retired lithium-ion batteries for electric vehicle with improved particle filter by H-infinity filter.* Energy Reports, 2023. **9**: p. 1937-1947.
37. Hong, J., et al., *Online joint-prediction of multi-forward-step battery SOC using LSTM neural networks and multiple linear regression for real-world electric vehicles.* Journal of Energy Storage, 2020. **30**.
38. Keil, J. and A. Jossen, *Electrochemical Modeling of Linear and Nonlinear Aging of Lithium-Ion Cells.* Journal of The Electrochemical Society, 2020. **167**(11).
39. Jiang, C., et al., *A state-of-charge estimation method of the power lithium-ion battery in complex conditions based on adaptive square root extended Kalman filter.* Energy, 2021. **219**.
40. Sun, Z., et al., *Min-max game based energy management strategy for fuel cell/supercapacitor hybrid electric vehicles.* Applied Energy, 2020. **267**.
41. Manoharan, A., et al., *Artificial Neural Networks, Gradient Boosting and Support Vector Machines for electric vehicle battery state estimation: A review.* Journal of Energy Storage, 2022. **55**.
42. Bonfitto, A., *A Method for the Combined Estimation of Battery State of Charge and State of Health Based on Artificial Neural Networks.* Energies, 2020. **13**(10).
43. Li, Y., et al., *A hybrid machine learning framework for joint SOC and SOH estimation of lithium-ion batteries assisted with fiber sensor measurements.* Applied Energy, 2022. **325**.
44. Li, S., et al., *Data driven battery modeling and management method with aging phenomenon considered.* Applied Energy, 2020. **275**.
45. Song, Y., et al., *A hybrid statistical data-driven method for on-line joint state estimation of lithium-ion batteries.* Applied Energy, 2020. **261**.
46. Dou, J., et al., *Extreme learning machine model for state-of-charge estimation of lithium-ion battery using salp swarm algorithm.* Journal of Energy Storage, 2022. **52**.
47. Vidal C., K.P., Naguib M., Malysz P., Gross O., Emadi A. , *Robust xEV Battery State-of-Charge Estimator Design Using a Feedforward Deep Neural Network.* SAE Int. J. Adv. & Curr. Prac. in Mobility, 2020. **2**(5): p. 2872-2880.
48. Darbar, D. and I. Bhattacharya, *Application of Machine Learning in Battery: State of Charge Estimation Using Feed Forward Neural Network for Sodium-Ion Battery.* Electrochem, 2022. **3**(1): p. 42-57.
49. Almaita, E., et al., *State of charge estimation for a group of lithium-ion batteries using long short-term memory neural network.* Journal of Energy Storage, 2022. **52**.
50. Wang, Y., et al., *A comprehensive review of battery modeling and state estimation approaches for advanced battery management systems.* Renewable and Sustainable Energy Reviews, 2020. **131**.
51. Tian, J., et al., *State-of-charge estimation of LiFePO4 batteries in electric vehicles: A deep-learning enabled approach.* Applied Energy, 2021. **291**.

52. Takyi-Aninakwa, P., et al., *An optimized relevant long short-term memory-squared gain extended Kalman filter for the state of charge estimation of lithium-ion batteries.* Energy, 2022. **260**: p. 1-15.
53. Chen, J., et al., *State of charge estimation of lithium-ion battery using denoising autoencoder and gated recurrent unit recurrent neural network.* Energy, 2021. **227**.
54. Ren, X., et al., *A method for state-of-charge estimation of lithium-ion batteries based on PSO-LSTM.* Energy, 2021. **234**.
55. Piao, N., et al., *Challenges and development of lithium-ion batteries for low temperature environments.* eTransportation, 2022. **11**.
56. Wang, Y.-X., Z. Chen, and W. Zhang, *Lithium-ion battery state-of-charge estimation for small target sample sets using the improved GRU-based transfer learning.* Energy, 2022. **244**.
57. Takyi-Aninakwa, P., et al., *An optimized long short-term memory-weighted fading extended Kalman filtering model with wide temperature adaptation for the state of charge estimation of lithium-ion batteries.* Applied Energy, 2022. **326**.
58. Oyewole, I., A. Chehade, and Y. Kim, *A controllable deep transfer learning network with multiple domain adaptation for battery state-of-charge estimation.* Applied Energy, 2022. **312**.
59. Ma, L., et al., *Robust state of charge estimation based on a sequence-to-sequence mapping model with process information.* Journal of Power Sources, 2020. **474**.
60. Lipu, M.S.H., et al., *Intelligent SOX Estimation for Automotive Battery Management Systems: State-of-the-Art Deep Learning Approaches, Open Issues, and Future Research Opportunities.* Energies, 2023. **16**(1).
61. Chen, Z., et al., *State of health estimation for lithium-ion batteries based on temperature prediction and gated recurrent unit neural network.* Journal of Power Sources, 2022. **521**.
62. Chen, J., et al., *SOC estimation for lithium-ion battery using the LSTM-RNN with extended input and constrained output.* Energy, 2023. **262**.
63. Chemali, E., et al., *State-of-charge estimation of Li-ion batteries using deep neural networks: A machine learning approach.* Journal of Power Sources, 2018. **400**: p. 242-255.
64. Weiss, K., T.M. Khoshgoftaar, and D. Wang, *A survey of transfer learning.* Journal of Big Data, 2016. **3**(1).
65. Liu, W., T. Placke, and K.T. Chau, *Overview of batteries and battery management for electric vehicles.* Energy Reports, 2022. **8**: p. 4058-4084.
66. Román-Ramírez, L.A. and J. Marco, *Design of experiments applied to lithium-ion batteries: A literature review.* Applied Energy, 2022. **320**.
67. Xiao, R., et al., *A novel estimation of state of charge for the lithium-ion battery in electric vehicle without open circuit voltage experiment.* Energy, 2022. **243**.
68. Xi, Z., et al., *Accurate and reliable state of charge estimation of lithium ion batteries using time-delayed recurrent neural networks through the identification of overexcited neurons.* Applied Energy, 2022. **305**.
69. Song, X., et al., *Combined CNN-LSTM Network for State-of-Charge Estimation of Lithium-Ion Batteries.* IEEE Access, 2019. **7**: p. 88894-88902.
70. Fasahat, M. and M. Manthouri, *State of charge estimation of lithium-ion batteries using hybrid autoencoder and Long Short Term Memory neural networks.* Journal of Power Sources, 2020. **469**.
71. Yang, X., et al., *Battery state of charge estimation using temporal convolutional network based on electric vehicles operating data.* Journal of Energy Storage, 2022. **55**.
72. Cui, Z., et al., *A hybrid neural network model with improved input for state of charge estimation of lithium-ion battery at low temperatures.* Renewable Energy, 2022. **198**: p. 1328-1340.